*minerals*

MDPI

*Article*

# High-Resolution Analysis of Fe–Mn Oxyhydroxide in Ferromanganese Nodules from the Northwestern Pacific Ocean and Insights on Element Mobility

**Chao Li [1], Weiyu Song [2,3,*], Zhenjun Sun [4], Wei Huang [2,3], Gang Hu [2,3], Xiaojun Yuan [2,3] and Shuh-Ji Kao [1,5,*]**

[1] State Key Laboratory of Marine Environmental Science, College of Ocean and Earth Sciences, Xiamen University, Xiamen 361102, China
[2] Qingdao Institute of Marine Geology, China Geological Survey, Qingdao 266237, China
[3] Laboratory for Marine Mineral Resource, Pilot National Laboratory for Marine Science and Technology (Qingdao), Qingdao 266237, China
[4] School of Earth Sciences, Institute of Disaster Prevention, Sanhe 065201, China
[5] State Key Laboratory of Marine Resources Utilization in South China Sea, Hainan University, Haikou 570228, China
* Correspondence: sweiyu@mail.cgs.gov.cn (W.S.); sjkao@xmu.edu.cn (S.-J.K.)

**Abstract:** Due to the multiple and poorly-crystallized phases in ferromanganese (Fe–Mn) nodules, research on the variability of micro-layers in nodules is limited and the accumulation of various elements with the growth of micro-layers have not been well documented. To address this gap, we examined the spatial distributions of elements in cross-sections of nodules from the Northwestern Pacific Ocean using in-situ electron microprobe analyses coupled with backscattered electron imaging and high-resolution X-ray elemental intensity mapping. Results suggest their significant selective enrichment of metal elements is similar to that of typical hydrogenetic nodules and diagenetic nodules. Moreover, $W_{Mn+Fe}$ of Fe–Mn oxyhydroxide is equal to 50% after normalization and Co and Ni show positive relationships with Mn/Fe ratio, suggesting Fe oxyhydroxide would serve as a diluter at exposed surface during nodule growth. In suboxic conditions, Mn, Ni, and Co start to release, and the remaining Fe oxyhydroxide may react with the surrounding sediment to form Si-rich layers. Our studies reveal the diverse growth processes and show a much larger chemical heterogeneity of individual layers, which extend the models about the mechanisms of chemical precipitation and environmental conditions that existed during nodule growth.

**Keywords:** ferromanganese nodules; hydrogenetic; electron microprobe analyses; high-resolution analysis

check for updates

**Citation:** Li, C.; Song, W.; Sun, Z.; Huang, W.; Hu, G.; Yuan, X.; Kao, S.-J. High-Resolution Analysis of Fe–Mn Oxyhydroxide in Ferromanganese Nodules from the Northwestern Pacific Ocean and Insights on Element Mobility. *Minerals* **2023**, *13*, 415. https://doi.org/10.3390/min13030415

Academic Editor: Francisco J. González

Received: 12 February 2023
Revised: 7 March 2023
Accepted: 14 March 2023
Published: 15 March 2023

**Copyright:** © 2023 by the authors. Licensee MDPI, Basel, Switzerland. This article is an open access article distributed under the terms and conditions of the Creative Commons Attribution (CC BY) license (https://creativecommons.org/licenses/by/4.0/).

## 1. Introduction

Marine ferromanganese (Fe–Mn) nodules are typically formed through accumulation of colloidal precipitates of iron–manganese oxide on the seafloor of the world's oceans [1,2]. Due to their slow growth rate and continuous adsorption and co-precipitation with a wide range of metals, Fe–Mn nodules may provide the records of long-term environmental variations, e.g., [3–5]. Routine bulk analysis of elements has advanced our understanding of their formation and interaction of metals with iron–manganese oxides. However, bulk compositions cannot provide an accurate means for supporting these inferences. Elements in Fe–Mn nodules are associated with one or more phases in Fe–Mn nodules [1,6,7]. Fe–Mn nodules are mainly composed of two components: disordered phyllomanganates (7-Å and 10-Å Mn oxides) and/or vernadite (δ-$MnO_2$), and Fe oxyhydroxide (δ-FeOOH, intergrown with $MnO_2$) [2,8,9]. In addition, nodules may contain calcite, apatite, goethite, quartz, and various aluminosilicates in minor amounts, the same ones that are found in sediments [6]. Other minor phases may also occur in Fe–Mn nodules (such as biogenic or residual biogenic phases). Besides the multiple phases, the secondary fillings (mainly Mn oxide and Fe

oxyhydroxide; the same phases with the main phase of Fe–Mn nodules) in the pore spaces, which are mostly the result of either diagenetic or hydrogenetic precipitates [10,11], can also alter the elemental contents greatly. Meanwhile, the high porosity (25%–61%), the large pore size, and the pore connectivity of nodules enable bottom seawater or pore water to enter the nodules constantly after nodule formation [1,11]. Thus, the inter-relations of metals in the Fe–Mn nodules are difficult to resolve by using bulk analyses.

Due to their fragile and poorly-crystallized phases, it is impossible to separate the main phases (Fe–Mn oxyhydroxide) from other phases in Fe–Mn nodules and crusts through microscope for chemical and mineral analysis. Also, the detection of minor minerals against a large burden of Fe–Mn oxyhydroxide cannot be exactly accomplished through direct mineralogical analysis. In order to address this question, sequential-leaching procedures that dissolve mineral phases of different stability step-by-step have been employed [6,7]. Systematic investigations of the leaching partitioning of 12 elements (major elements; Mn, Fe, Co, Ni, Zn, Cu, Pb, Ti, Al, Si, Ca, P; [6]) and 40 elements (mainly minor and trace metals; [7]) between the main mineral phases were carried out. However, problems of incomplete selectivity for the discrete phases and variable reproducibility may influence interpretations of sequential-leaching results. Meanwhile, although the sequential-leaching procedures can separate multiple phases, the interference of secondary fillings still cannot be avoided.

In order to reconstruct geological and oceanographic signatures from slow-growing Fe–Mn nodules, it is crucial to provide a reliable fine-scale element variation pattern for each sample since the nanometer- to micrometer-thick layers of the Fe–Mn nodules are reflecting different formation processes [12]. In recent years, several studies focused on high-resolution analyses of the individual layers within the nodules, e.g., [10,13,14]. The detailed in-situ studies revealed the diverse growth processes and showed much larger chemical heterogeneity of individual layers. However, they focused on diagenetic nodules from Clarion and Clipperton Zone and Peru Basin. Small-scale distribution patterns, chemical diversity and variability, and genetic controls recorded in hydrogenetic Fe–Mn nodules have not been well documented yet.

Here, we conducted a high-resolution and continuous geochemical study for three hydrogenetic nodules collected from the Northwestern Pacific Ocean to explore the element precipitation behavior and, further, (1) better evaluate the controls on the economic potential of ferromanganese deposits; and (2) accurately decipher oceanographic and climatic records locked in hydrogenetic Fe–Mn nodules. We examined the spatial distributions of major elements in cross-sections of the nodules using in-situ electron microprobe analyses (EMPA) coupled with backscattered electron imaging (BSE) and high-resolution X-ray elemental intensity mapping. Our data mostly prove and further extend the models of others about the mechanisms of chemical precipitation and environmental conditions that existed during nodule growth.

## 2. Materials and Methods

### *2.1. Sample Preparation*

The D07 nodule was collected by the R/V *Hai Yang Liu Hao* in 2017, and the FND-11 and FND-49 nodules were collected by the R/V *Hai Da Hao* in 2020 (Figure 1). The locations and depths of the three nodules are shown in Table S1 in the Supporting Information. The three nodules occurred at the soft sediment surfaces (in the upper 2–3 cm of the sediments; the mixture of sediment and bottom seawater) and were sampled with box samplers. D07 has a spheroidal shape with a size of ~2 cm ferromanganese layers, while FND-11 and FND-49 have ellipsoidal shapes with ~0.7–1.2 cm and ~0.8–1.2 cm thick ferromanganese layers, respectively (Figure S1 in the Supporting Information). The three nodules were fully impregnated with epoxy resin under vacuum conditions. They were then cut into three pieces, with the cut direction vertical to the layers. The middle parts were attached to a micro slide with resin and the other side was polished to produce a thin section. The thin sections were 600 μm thickness and were then placed in a SC701C Quick Carbon Coater

and coated with a film of carbon for the scans and chemical analyses. In addition, the other two parts were subsampled using a microdrill with a 0.25 mm diameter to obtain samples of sub-layers along a profile perpendicular to the layers in order to determine the concentrations of the trace elements, including the rare earth elements plus yttrium (REY), in the nodules.

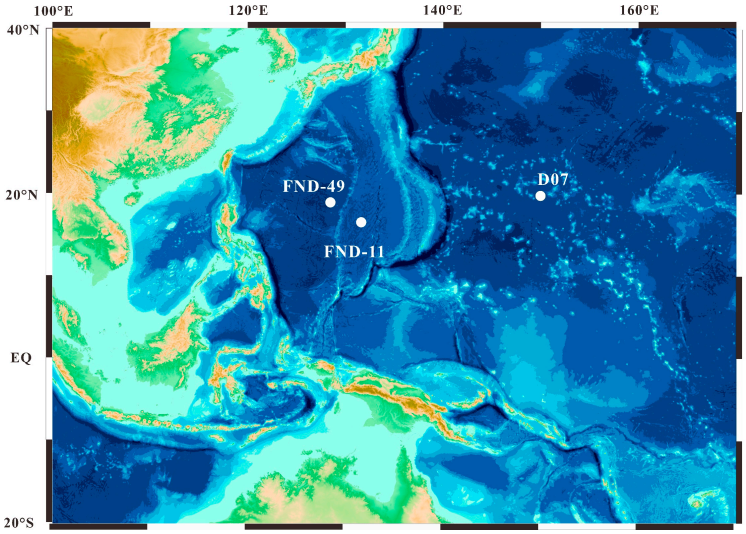



**Figure 1.** Location map for this study. The white circles are sites FND-11, FND-49 and D07.

### *2.2. Analytical Methods*

#### 2.2.1. BSE Images and High-Resolution X-ray Elemental Intensity Mapping

For detailed investigation of the growth structures of individual layers within the nodules, BSE images of the nodules were taken using a JEOL JXA-8230 electron microprobe at the Hebei Key Laboratory of Earthquake Dynamics, China.

High-resolution X-ray elemental intensity mapping for Mn, Fe were applied for Fe–Mn oxyhydroxide on carbon-coated thin sections. The X-ray mapping was carried out using a JEOL JXA-8230 electron microprobe at the Hebei Key Laboratory of Earthquake Dynamics, China. The operation conditions of an accelerate voltage of 15 kV, a probe current of 50 nA, and a beam size of 1 to 5 μm were adopted for mapping. The dwell time was set to be 50 ms for each point.

#### 2.2.2. EMPA Spot Analysis

EMPA spot analysis requires precise knowledge of the sample geometry (layers and what elements are present in each layer [15]). We applied BSE images and X-ray Mn and Fe intensity maps (Figures 2a–c, 3a–c and S2a–c) to examine the meandering growth microstructure layers of the nodules and clarified what elements should be contained in hydrogenetic nodules and crusts through other literature (Cook Islands) [16]. Then, we measured K, Ti, Ca, P, Pb, Na, Mg, Al, Si, Mn, Fe, Co, Ni, and Cu along the growth direction pointing specifically on positions where Fe–Mn oxides are dense, surface flat and well formed (surface to be normal to the electron beam) to ensure the accuracy of the tests. Major elements of Fe–Mn oxyhydroxide were determined using a JEOL JXA-8230 electron microprobe at the Hebei Key Laboratory of Earthquake Dynamics, China. The individual layers were measured with a focused 1μm beam. The counting times for the analyzed elements were 10 s for Mn, Fe, Ni, Cu, Na, Mg, Al, Si, K, Ca, Ti, P; 45 s for Pb; and 50 s for Co. Rhodochrosite (Mn), haematite (Fe), cobaltite (Co), synthetic $Ni_2Si$ (Ni), cuprite (Cu), albite (Na), kaersutite (Mg, Al, Si), biotite (K), apatite (Ca, P), rutile (Ti), and krokoite (Pb) were used as standards (SPI standards).

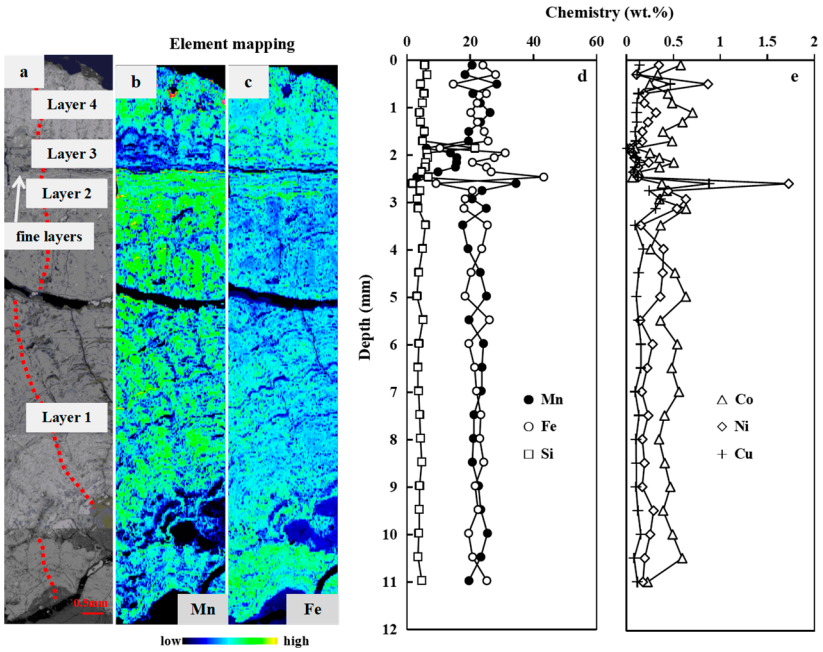



**Figure 2.** Microscopic investigations and depth profiles of element contents of FND-11. (**a**): BSE image; (**b**,**c**): X-ray Mn and Fe intensity maps; (**d**,**e**): Depth profiles of Mn, Fe, Si, Ni, Cu, and Co content. The red dashed line in (**a**) is the test line of EMPA.

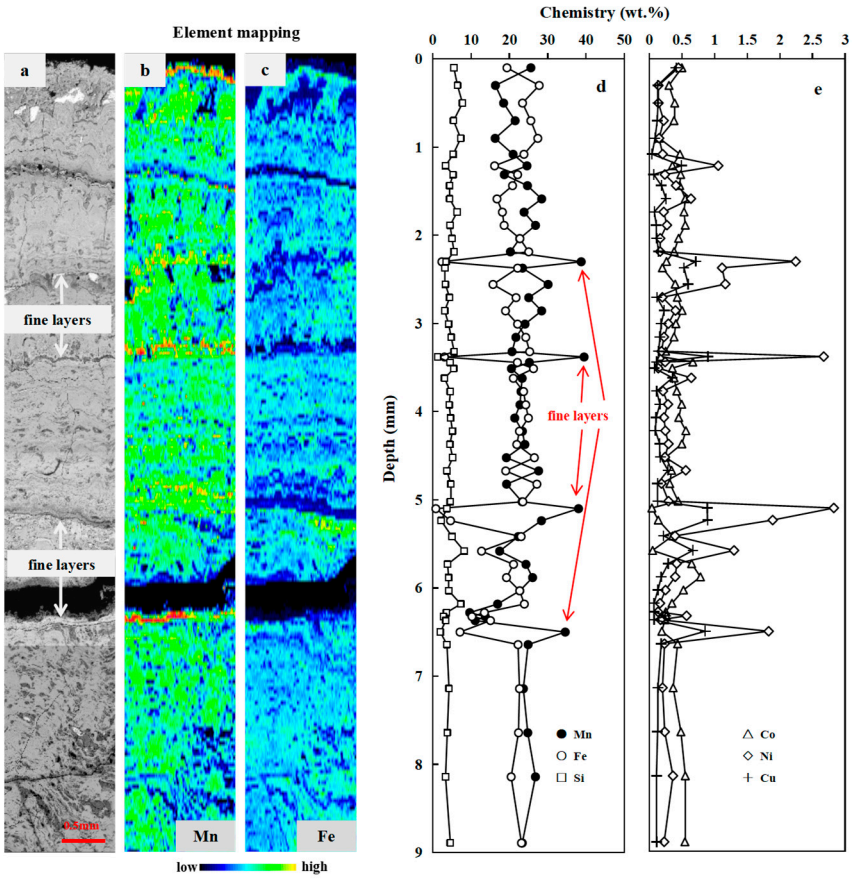



**Figure 3.** Microscopic investigations and depth profiles of element contents of FND-49. (**a**): BSE image; (**b**,**c**): X-ray Mn and Fe intensity maps; (**d**,**e**): Depth profiles of Mn, Fe, Si, Ni, Cu, and Co content. (Microscopic investigations and depth profiles of element contents of D07 are available in the Supporting Information.).

#### 2.2.3. ICP-MS Analysis

In order to know more about the genetic origins of the three nodules, trace elements including rare earth elements (REEs) of individual layers were analyzed at Yanduzhongshi Geological Analysis Laboratories, China, by using inductively coupled plasma–mass spectrometry (ICP-MS), with a 0.01–0.1 μg/mL detection limit. The dissolution procedure was as follows: 50 milligrams of sample powder was digested in a Teflon bottle with 1 mL of HF, 1 mL of $HNO_3$, and 1 mL of HCl, then heated on an electric hotplate and steamed at 190 °C for 48 h. Then, 1 mL $HNO_3$ was added and the sample was evaporated again to remove residual hydrochloric and hydrofluoric acids. After these processes, 4 mL of $HNO_3$ (20%) and 0.5 mL of Rh (μg/mL) internal standard solutions were added; the mixture was heated at 150 °C for 12 h. After cooling to approximately 25 °C, 1–2 drops of hydrogen peroxide were added and transferred to a disposable plastic bottle containing 2% $HNO_3$, diluted 2000×, and analyzed using ICP-MS.

## 3. Results

### *3.1. Individual Layers*

Individual layers were analyzed to better define growth processes as well as to determine genesis changes within nodules. BSE images and high-resolution X-ray Mn and Fe intensity maps of the nodules show that they exhibit complex internal structures (Figures 2a–c, 3a–c and S2a–c). Microprobe analyses and geochemistry identified several types of concentrically and irregularly banded μm to mm thick layers of Mn-oxide/Fe-oxyhydroxide material in all studied nodules. These layers vary in density, continuity, reflectivity, and chemistry.

#### 3.1.1. FND-11

Microscopically as well as chemically, four different sub-layers of nodule growth can be distinguished (Figure 2; Table S2 in the Supporting Information). Layer 1 and Layer 4 are characterized with mottled texture and display similar geochemical characteristics. The mean Fe/Mn ratio is 0.98 (range 0.59–1.94). The chemical composition of the two layers combined (n = 25), except for one point with high Si content (21.44%), expressed as mean wt.% (min%–max%) was 2.24% Ca (1.89%–2.57%), 22.12% Mn (17.60%–28.40%), 22.51% Fe (14.62%–27.99%), 0.39% P (0.28%–0.48%), 1.16% Mg (0.82%–2.48%), 1.57% Al (1.27%–2.05%), 4.45% Si (3.14%–6.34%), 0.45% Co (0.22%–0.70%), 0.25% Ni (0.11%–0.87%), and 0.13% Cu (0.08%–0.47%). Layer 2 and Layer 3 consist of dense and laminated growth pattern, with a higher chemical variability. The Fe/Mn ratio ranges from 0.07 to 3.77. The chemical composition of the two layers combined (n = 10) expressed as mean wt.% (min%–max%) was 1.77% Ca (0.89%–2.48%), 17.71% Mn (3.09%–34.47%), 24.05% Fe (9.15%–43.24%), 0.36% P (0.19%–0.51%), 1.31% Mg (0.58%–3.76%), 1.85% Al (1.31%–2.21%), 4.84% Si (1.72%–6.71%), 0.34% Co (0.06%–0.63%), 0.41% Ni (0.06%–1.73%), and 0.24% Cu (0.07%–0.88%).

#### 3.1.2. FND-49

Mottled texture layer is the most common layer type in FND-49 (Figure 3), with Mn/Fe ratios approximate to 1 (1.08 ± 0.29 wt.%, n = 48; Table S3). The characteristics of element contents are almost the same with Layer 1 and Layer 4 of FND-11.

Moreover, several fine, μm-thick veins of high reflectivity can be detected within the mottled texture layer (Figure 3). The veins are characterized by dense and laminated growth pattern. They display high reflectivity, with extreme high Mn/Fe ratios (4.9–46.5 wt.%) and high Ni (2.09–3.33 wt.%) and Cu (0.80–1.06 wt.%) contents but low Co (0.0445–0.30 wt.%).

#### 3.1.3. D07

Four different sub-layers of nodule growth can be distinguished and each sub-layer has distinct and variable chemical compositions (Figure S2; Table S4 in the Supporting Information). Layer 1 is dense, with a columnar growth pattern and has relatively high Mn/Fe ratios (2.45 ± 0.38, n = 26) accompanied by high Co contents (0.93 ± 0.13 wt.%, n = 26) and Ni con-

tents (0.68 ± 0.16 wt.%, n = 26). Layer 2 is characterized with mottled texture which is common for hydrogenetic Fe–Mn crusts, displaying lower Mn/Fe ratios (1.21 ± 0.23 wt.%, n = 18) and slightly lower Co contents (0.55 ± 0.22 wt.%, n = 18). Layer 3 (<0.5 mm in thickness) consists of dense and laminated growth pattern displaying low reflectivity, which usually represents slow growth, with higher Fe concentrations and low Mn/Fe ratios (0.12–0.67, n = 2). Moreover, one ~60 μm-thick layer with high Mn/Fe ratio (Mn/Fe = 6.4) can be detected within Layer 3, which is similar to the several small, μm-thick veins in FND-49. Layer 4 is similar to Layer 2, macroscopically characterized with mottled texture, but with a higher chemical variability (Mn = 4.17–23.26 wt.%, Fe = 8.80–30.14 wt.%, Co = 0.16–0.78 wt.%, Si = 3.87–16.02 wt.%). In Layer 4 some measured points have relatively low Mn and/or Fe contents, attributed to spotting on porous structure or Si-rich micro-layers.

### *3.2. Rare Earth Elements Plus Yttrium*

Table S5 in the Supporting Information shows REY statistics for individual layers. REY exhibited a high content of 1280–2168 ppm (mean 1841 ppm), especially for Ce (654–1448 ppm). The high Nd content (146–227 ppm), low $(Y/Ho)_{SN}$ (SN: Post-Archaean Australian shale-normalized, PAAS; Mclennan, 1989) ratios (0.63–1.04), and positive Ce anomaly ($Ce_{SN}/Ce^*_{SN}$ = 1.82–4.15, mean 2.66) showed that the nodules were hydrogenous origin [1,2,16,17]. In addition, the nodules showed no or weakly positive Eu anomalies ($Eu_{SN}/Eu^*_{SN}$ = 1.00–1.15, mean 1.07), which indicates an oxidizing environment and excludes hydrothermal processes [17–19]. For comparison, Figure 4 shows the REY distributions for Fe–Mn deposits from different areas [1,16]. All samples from the three nodules in this study have similar REY distributions with hydrogenetic nodules from Cook Islands.

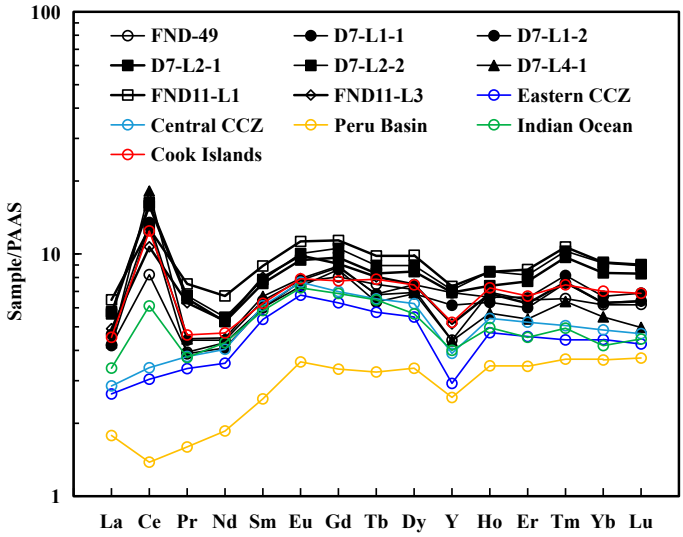



**Figure 4.** Post-Archaean Australian shale (PAAS)-normalized [20] rare earth element and yttrium (REY) distribution patterns of each layer using the ICP-MS analysis data of each layer. The negative Ce anomaly occurs in every individual layer. Other data are taken from Hein and Koschinsky (2013) and Hein et al. (2015) [1,16].

## 4. Discussion

### *4.1. Microscopic Growth Structure Co-Varies with Mn/Fe Ratio*

Different growth structures show various Mn/Fe ratios. In general, columnar growth pattern has relatively high Mn/Fe ratios (average 2.45), mottled texture layer displays moderate Mn/Fe ratios (0.8 < Mn/Fe < 1.2), dense and laminated growth pattern are of low Mn/Fe ratios (Mn/Fe < 0.8), while fine layers tend to have extremely high Mn/Fe ratios (4.9–46.5) (Figures 2, 3 and S2). These findings demonstrate a strong relationship between composition and growth structure in the Fe–Mn nodules. Moreover, individual growth features tend to have the high Mn concentrations in their interior, with Mn concentrations decreasing on the margin of growth columns (Figure 5). Lower Mn concentrations in the

external parts may suggest the leaching of Mn out of this part. It corresponds to the Fe-rich character of the filling materials. Fe concentration tends to vary inversely with Mn within these individual growth features. In contrast with individual growth features, the fillings in pore space have higher concentrations of Fe, and correspondingly low Mn/Fe ratios. This distribution of Fe suggests that Fe minerals occur as both a co-precipitate with Mn oxides and as a cement for the main Fe–Mn phases.

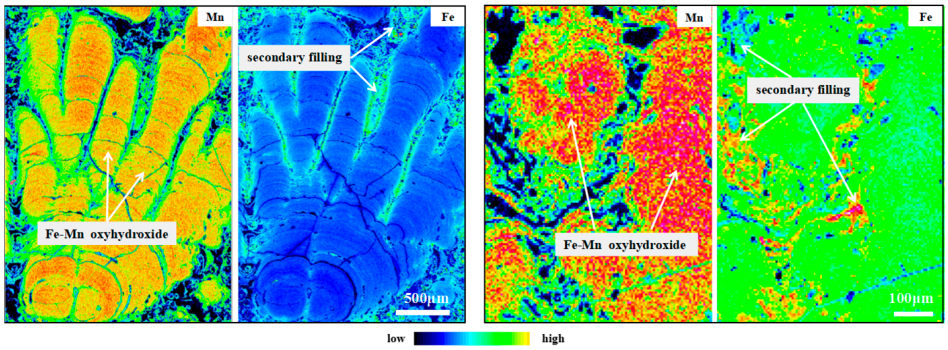



**Figure 5.** High resolution X-ray elemental intensity mapping of Layer 1 (**left**) and Layer 2 (**right**) of D07.

### *4.2. Advantage of High-Resolution EMPA In-Situ Test*

In-situ tests specifically on dense Fe–Mn oxides by using EMPA allow us to avoid the interference from secondary fillings and other mineral phases to a great extent. Mn and Fe show a nice inverse relationship and the contents of Mn and Fe, though varying in a wide range, sum to about 45% (Figure 6a). In contrast, due to the interference of matrix, Mn and Fe in the bulk composition reported previously are significantly lower than the results from EMPA, amounting to ~35% and ~27%, while the inverse relationships between Mn and Fe show much scattering (Figure 6a; the locations and depths of samples from other literature are shown in Table S1).

The Fe–Mn oxides contain high water content within their crystal structure (vernadite ~16–25 wt.%; todorokite and phyllomanganates ~10–13 wt.%) [21–23]. Meanwhile, EMPA analysis is also affected by the porosity of the growth structures [10]. Due to these two facts, the analytical sums of EMPA often are well below 100%. Thus, we normalize chemical data to 100% total oxides (0% water and 0% pore space) as compositions normalized may be more meaningful in comparison in this paper. Since EMPA cannot detect $H_2O$, other major oxides in hydrogenetic nodules Equation (1) were all measured [16], and then we adjusted percent weight of every individual element by recalculation via adding up all measured metal oxides as 100%:

$$W_{total} = W_{K_2O} + W_{CaO} + W_{TiO_2} + W_{P_2O_5} + W_{PbO_2} + W_{Na_2O} + W_{MgO_2} + W_{Al_2O_3} + W_{SiO_2} + W_{MnO_2} + W_{Fe_2O_3} + W_{NiO} + W_{Co_2O_3} + W_{CuO} \quad (1)$$

$$W^n{}_x = W_x / W_{total} \times 100 \quad (2)$$

where $W_x$ is the measured weight of a given element, Wtextsuperscript$n_x$ is adjusted percent weight of the element. Note that although the summatory of the major oxides (oxides in Equation (1) and $H_2O$) in this study could never be 100%, it has been demonstrated that the remaining elements (As, Au, Ag, B, Be, Bi, Br, Ba, Cl, Cd, Cs, Ga, Cr, Hf, Hg, In, Ge, Li, Nb, Rb, Mo, Sc, Se, Sb, Sr, Ta, Sn, Te, Tl, Th, V, W, Y, U, Zn, Zr, La, Ce, Pr, Nd, Sm, Eu, Gd, Tb, Dy, Ho, Er, Tm, Yb, Lu, Ir, Os, Pd, Pt, Rh, Ru) added up to about 1% in hydrogenetic nodules [16], suggesting the effects of trace elements on normalization are more minor than that of water and pore space. Therefore, after normalization, EMPA geochemistry could provide an excellent approximation (about 99%) of the metal contents. After removing the interference from water and pore space, the $W_{Mn+Fe}$ is equal to 50% for almost all data points except some data with high Si contents. The 50% for $W_{Mn+Fe}$ derived

by EMPA after the normalization (0% water and 0% pore) (Figure 6b) is consistent with the characterization of the 'pure crust' ($W_{Mn+Fe}$ equal to 50% after normalization of whole rock samples to hygroscopic-moisture-free, 110 °C overnight, basis) proposed by Manheim and Lane-Bostwick (1988) [24]. The result indicates the element contents of Fe–Mn nodules can be accurately obtained by EMPA.

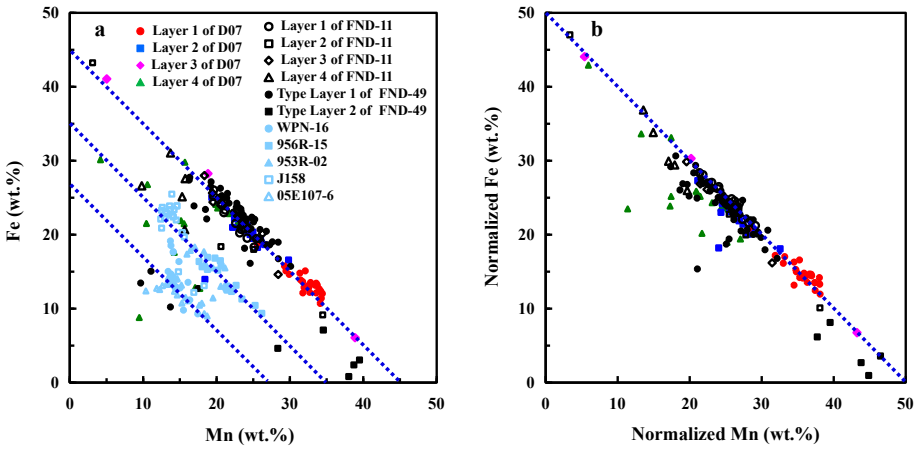



**Figure 6.** (**a**): Scatter plot for Fe vs. Mn; (**b**): Scatter plot for normalized Fe vs. normalized Mn. The element contents from other literature were obtained through whole rock analysis [3–5,25].

### *4.3. Geochemical Composition and Genetic Classification*

The three nodules are mainly composed of columnar and/or mottled growth patterns (Figures 2a, 3a and S2a), similar to the hydrogenetic nodules from the Cook Islands and hydrogenetic crusts from the Western Pacific [16,26]. Geochemical analyses yielded low Mn/Fe ratios (<3) and low Ni (379–15659, average 3932 ppm) and Cu (104–8035, average 1806 ppm) contents but high Co (1635–12777, average 5842 ppm) and REY (1280–2168 ppm, average 1841 ppm) contents (Tables S2–S5) in these columnar and mottled layers, which is also similar with the hydrogenetic nodules and crusts [16,26] and are far different from diagenetic nodules from the CCZ and PB [10,14].

The most common scheme to constrain the genetic types for ferromanganese nodules is the Fe–Mn–(Cu + Ni + Co) × 10 ternary diagram which classifies the nodules as hydrogenetic, diagenetic, and hydrothermal based on their modes of origin [27]. On the basis of this ternary diagram (Figure 7a,b), points of columnar and mottled layers mostly are of hydrogenetic type. Bau et al. (2014) proposed two easy-to-use yet robust discrimination diagrams based on geochemical relationships controlling the rare earths and yttrium (REY) inventory of marine Fe–Mn oxide deposits [28]. Nodules in this study have negative Y ($Y_{SN}/Y^*_{SN}$ = 0.63–0.98), positive Ce ($Ce_{SN}/Ce^*_{SN}$ = 1.82–4.15) anomalies, and an Nd content 138.7–227.5 mg $kg^{-1}$, showing that all nodules are of typically hydrogenetic origin (Table S5). The REY plots fall mostly within the hydrogenetic field (Figure 7c,d).

These data, including the micro-texture and geochemistry, suggest that the three nodules have been mostly forming from hydrogenetic precipitation. Note that some points of layer 1 of D07 plotted within mixed hydrogenetic-diagenetic type. It seems that single layers of the nodules have a wider spread within this ternary diagram than the respective bulk nodules [10]. Therefore, the in-situ chemical composition must be interpreted with care when inferring the genesis of the nodules.

Moreover, as described before, several fine, μm-thick veins of high reflectivity can be detected within mottled layers of FND-49 and D07 (Figures 3 and S2). The fine layers yielded extreme high Mn/Fe ratios (4.9–46.5) and high Ni (7155–30,049 ppm) and Cu (4112–10,090 ppm) contents but low Co contents (425–4112 ppm), which is similar with diagenetic nodules from the CCZ and PB [10,14]. The element characteristics indicate that the fine layers are of diagenetic origin. The layers fall mostly within the diagenetic field using Fe–Mn–(Cu + Ni + Co) × 10 ternary diagram (Figure 7a,b).

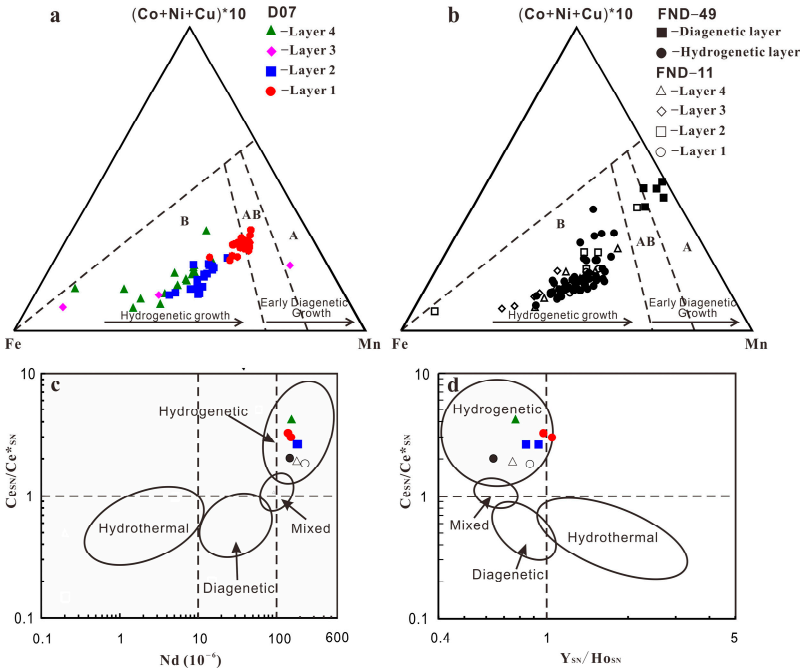



**Figure 7.** (**a**,**b**): Ternary diagram for genesis of ferromanganese deposits from Bonatti et al. (1972) [27]. Dashed black lines border the three nodule type fields. A: diagenetic nodules, AB: mixed type nodules, and B: hydrogenetic nodules and crusts. All data plotted as wt.%; (**c**,**d**): Discrimination diagrams based on geochemical relationships from Bau et al., 2014 [28]. All major element contents in these pictures and later pictures below are normalized data.

### *4.4. Element Accumulation in Fe–Mn Nodules and Environmental Conditions*

Element correlations of Fe–Mn oxides from this study are shown in Figures 8–10. The results indicate that colloid-chemical model described by Koschinsky and Halbach (1995) is valid for our results here [6]. Anionic species and large complexes with low charge densities (e.g., P and Si; Figures 8a–c and 10a) show a higher affinity to slightly positive Fe oxyhydroxide colloids while hydrated cationic species such as $Ca^{2+}$ and $Mg^{2+}$ are preferentially sorbed on the negative surface of Mn oxides (Figures 8e,f and 9d,e). In addition, the low charge density of the FeOOH surface enables the formation of covalent bonds with other slightly charged or neutral dissolved species, including $Ti(OH)_4^0$ (Figure 8d) [29]. Moreover, our results reveal more correlations of the elements (e.g., Co, Ni, Cu, Si, and Mn) and environmental conditions that existed during nodule growth, as discussed below.

#### 4.4.1. The Diverse Precipitation Processes of Co, Ni, and Cu

Typically, hydrogenetic layers have similar amounts of Fe and Mn and high Co content, whereas layers produced from diagenesis have high Mn/Fe ratios and high Ni and Cu contents but low Co content (Figure 9a–c). Hydrogenetic precipitation is driven by the oxidation of dissolved $Mn^{2+}$ and $Fe^{2+}$ in oxygen-rich ocean waters [6,12]. The high concentrations of Co result from oxidation on the surface of δ-$MnO_2$ particles [6,29]. Co exists in seawater mainly as a hydrated divalent cation and is, therefore, adsorbed by hydrous $MnO_2$ colloids combined with an oxidation to $Co^{3+}$ after outer sphere adsorption (oxidative scavenging) [30]. Thus, Co is considered to be an element most characteristic of hydrogenetic precipitation. On the other hand, diagenetic precipitation occurs within the pore space of deep-ocean sediments [31,32]. The mineral phases of diagenetic nodules typically incorporate metal ions such as $Ni^{2+}$, $Cu^{2+}$ and to balance negative charge deficits in their crystal lattice [1,10,33]. The points of hydrogenetic layers adjacent to diagenetic layers seem to be influenced by diagenesis as their Cu and Ni contents are higher than that of other hydrogenetic points (Figure 9d–f).

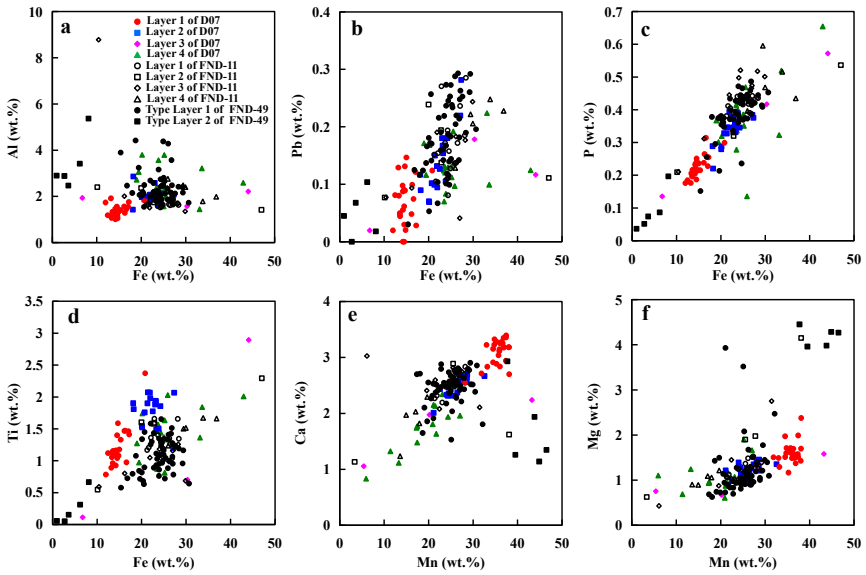



**Figure 8.** (**a**–**d**): Relationships of Fe with Al, Pb, P, and Ti; (**e**,**f**): Relationships of Mn with Ca and Mg.

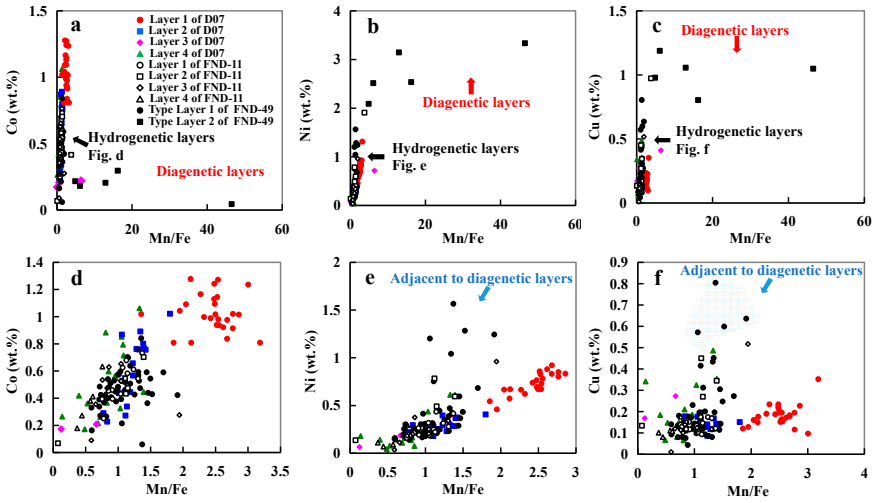



**Figure 9.** (**a**–**c**): Relationships of Mn/Fe with Co, Ni, and Cu of all points in the nodules; (**d**–**f**): Relationships of Mn/Fe with Co, Ni, and Cu of points in the hydrogenetic layers.

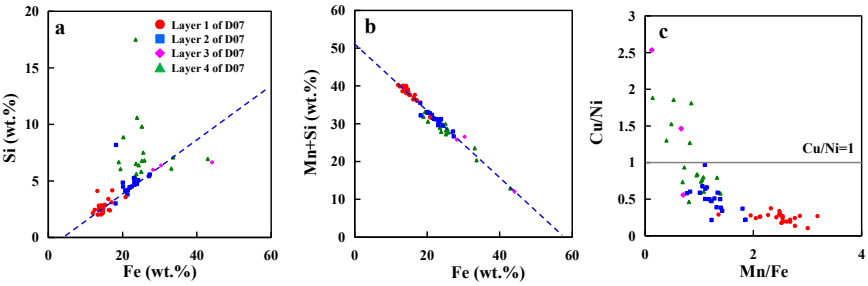



**Figure 10.** (**a**,**b**): Si and Mn+Si versus Fe; (**c**): In Si-rich layers Cu > Ni.

Previous studies suggest that $MnO_2$ colloid particles which have strong negative surface charges at the seawater pH of ~8 adsorb dissolved cations such as $Ca^{2+}$, $Mg^{2+}$, $Co^{2+}$, and $Ni^{2+}$ [6,7]. In hydrogenetic layers, $Ca^{2+}$, $Mg^{2+}$ are positively related to Mn content (Figure 8e,f). However, Co and Ni are positively related to Mn/Fe ratio, rather than Mn content (Figure 9d,e). This difference between $Ca^{2+}$, $Mg^{2+}$, and $Co^{2+}$ and $Ni^{2+}$ precipitation may be controlled by the different processes of absorption. It seems that $Ca^{2+}$,

$Mg^{2+}$ are adsorbed by $MnO_2$ colloid particles in seawater (before $MnO_2$ colloid and FeOOH particles combination), whereas $Co^{2+}$ and $Ni^{2+}$ are adsorbed by Fe–Mn oxyhydroxide at the surface of nodules (after $MnO_2$ colloid and FeOOH particles co-precipitation). Fourier-transformed infrared spectroscopy and transmission electron microscopy revealed that Ni and Co are incorporated in the octahedral sheets of phyllomanganates or in todorokite, suggesting Ni and Co are absorbed by the mineral phases rather than the $MnO_2$ colloid in the seawater [34]. The constant occupation of Fe + Mn of ~50% (Figure 6b) as mentioned earlier suggests that concomitant Fe precipitation would serve as a diluter at the surface of nodules. This phenomenon was also observed in the hydrogenetic crusts on the Western Pacific Takuyo-Daigo Seamount [25].

As mentioned above, $MnO_2$ can take up many different cations. However, Cu content in the three nodules does not have a good linear relationship with Mn or Mn/Fe ratio (Figure 9f). The amount of Cu incorporated into the nodules does not appear to be dependent on the crystal structure or on the Mn content of the mineral phase. Cu appears to be controlled by the different availability of the respective metal due to varying environmental conditions [10]. One of the major differences between the diagenetic nodules from the CCZ and the PB is the Cu content, which is distinctly lower in PB nodules. Wegorzewski and Kuhn (2014) assumed that this difference may be controlled by the different composition of the sediments in both regions [10].

#### 4.4.2. The Anomalous Fine Layers: Diagenesis and High Biological Productivity

As described in the previous section, several fine diagenetic layers can be observed within the mottled texture layer. Different from the other layers, the fine layers yielded extreme high Mn/Fe ratios and high Ni and Cu contents but low Co contents, which is similar to diagenetic nodules from the Peru Basin. Hydrogenetic layers form as a result of element precipitation from oxygen-rich seawater [6,7,12], whereas diagenetic layers form as a result of element precipitation from underlying suboxic pore water [1,8,35,36]. In order to produce near-surface, suboxic conditions in sediments it would be necessary to increase the organic carbon flux to the seafloor, as is the case in the Peru Basin today [2,37]. Oxidation of organic matter in underlying sediments results in the reduction and dissolution of Mn oxides and release of associated elements (Ni, Cu, among others) [2,9]. These metals diffuse upwards and, on contact with oxygen-rich water, are reoxidized, leading to the precipitation of 7-Å and 10-Å Mn oxides (disordered phyllomanganates; diagenetic layers) [9,30]. Thus, diagenetic layers reflect climatically induced variations in surface-water biological productivity, as well as raised suboxic conditions in the underlying sediments [2,9,30]. The diagenetic layers within the nodules still grew in oxic condition, but the oxic and suboxic front in the sediment raised (near the bottom of the ferromanganese nodule) due to the high organic matter supply, which is also proposed by Heller et al. (2018) and Su et al. (2022) [14,38].

#### 4.4.3. The Si-Rich Layer and the 'Cu > Ni Problem': Suboxic Condition

Si shows a significantly positive correlation with the Fe-oxyhydroxide (Figure 10a). Si in nodules are not only present in refractory detrital fractions, but are also leachable with the Fe–Mn oxides [6,19]. This leachable Si may derive mainly from Si colloidal phases precipitated from seawater and adsorbed on FeOOH colloids [19,39]. Our analyses demonstrate that the Si/Fe ratios are always the same in D07, whereas Si/Fe ratios of some points in Layer 4 of D07 are relatively high (Figure 10a). The most prominent features of this Si-rich layer type are the high Si content, the low Mn content and the strong depletion of Ni, Cu, and Co (Figures S2 and 10). However, Fe contents of the Si-rich layer are normal compared to the other hydrogenetic layers (Figures S2c,d and 11). The same pattern is also reported from buried manganese nodules from Clarion-Clipperton Zone [38]. They found nodules subject to suboxic conditions are reductively dissolved and react with the surrounding sediment and pore water. Under suboxic conditions, $Mn^{4+}$ reduction occurs [40]. Mn(IV) oxides are unstable and are reduced, whereas Fe(III) oxyhydroxides

remain stable [41,42]. The hydrogenetic layers start to dissolve and the associated metals such as Mn, Ni, Co, and Cu are released into the pore water or seawater. The remaining Fe oxyhydroxides probably react with products of the dissolution of siliceous ooze and clay minerals to form the Si-rich layer. This indicates that the Si-rich layer in D07 formed in suboxic condition. Moreover, the nice relationship between $W_{Mn+Si}$ and $W_{Fe}$ in the Si-rich layer of D07 indicates Si colloidal cover the vacancies leaving after $MnO_2$ dissolution (Figure 10b).

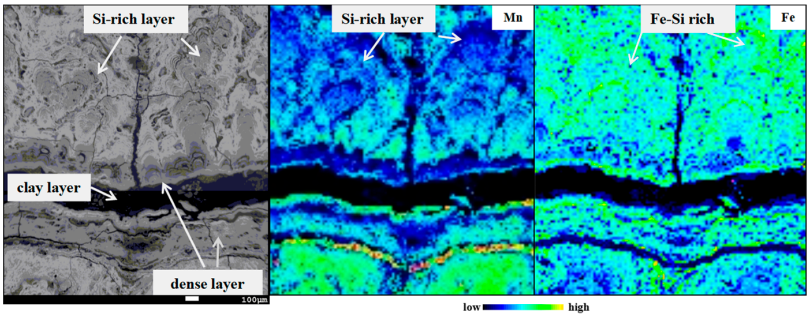



**Figure 11.** Si-rich layer in the layer 4 of D07.

Increased sedimentation rates of the surrounding marine sediment may lead to the suboxic generation of the nodule. A nodule (WPN-16) near the D07 location site has been reported [5]. The element contents of each individual layer of WPN-16 were measured through XRF and ICP-MS. Unfortunately, Si contents were not tested in the study. Nevertheless, the two nodules (D07 and WPN-16) have the same microstructures and similar variation ranges for other elements (e.g., Mn, Fe), which mean they grew in the same environments. The age of the outmost layer of WPN-16 (Fe-rich and Mn-less, the same characteristics with Si-rich layer in this study) is ~3.6–0 Myr [5], which corresponds with a period of enhanced eolian dust and loess accumulation in the Japan Sea (ODP Site 885/886 and ODP U1430) and in North China [43–45]. Since the nodule site is located along the westerly path, as are the Japan Sea and North China [5], it is possible that either the nodules around D07 were buried and the $MnO_2$ was destroyed in suboxic sediments after burial, or the seafloor became suboxic with the enhanced dust fluxes and increased organic matter deposition associated with higher primary productivity. In both cases, the oxic–suboxic front raised above the nodules, causing the release of Mn, Ni, Co, and Cu into the pore water or seawater under suboxic conditions. Our observations suggest the latter case is more possible as the nodules still occur in the upper 2–3 cm of the sediment column in the present day or, even if the nodules were buried, they were possibly buried in the near-bottom sediment and were subsequently exposed on the seafloor. Furthermore, global cooling during the period of ~3.6–0 Myr may have contributed to sluggish ocean circulation and enhanced ocean stratification, which could have reduced the transfer of organic carbon and nutrients to the seafloor from the euphotic zone [46]. After the suboxic generation, seafloor became oxic again and the nodule grew by hydrogenetic precipitation under oxic conditions in the upper 2–3 cm of the sediment column (recent).

Moreover, our analyses demonstrate that the Cu/Ni ratio is always <1, whereas in Si-rich layer it is always >1 (Figure 10c). This is also consistent with the characteristics of oxic generations and suboxic generations(the Cu/Ni ratio is always <1 in surface nodules, whereas in buried nodules it is always >1) [38]. Cu may be reincorporated into the suboxic generations whereas $Ni^{2+}$ mobilized during Mn oxide dissolution stays in solution and diffuses away from the dissolution site [47]. In addition, the fraction of Cu which was released during Mn(IV) oxide reduction may adsorb to either the clay or Fe oxide fraction, which is probably not the case for dissolved $Ni^{2+}$ [13].

### *4.5. Formation of Hydrogenetic Nodules*

Figure 12 shows a model for the formation of the different layers in the three Fe–Mn nodules. For the formation of hydrogenetic layers, a two-stage colloid-chemical model (Figure 12a,b) is proposed. Stage one describes processes taking place in the water column which include formation of colloidal phases and scavenging of other elements. Under normal Eh–pH conditions of seawater (Eh > 0.5 V; pH~8), manganese tends to oxidize to $MnO_2$ and iron to FeOOH [6,7,9]. $MnO_2$ has a strong negative surface charge and FeOOH has a slightly positive surface charge. Thus, the negatively charged $MnO_2$ colloid particles adsorb dissolved cations such as $Ca^{2+}$, $Mg^{2+}$ and the slightly positively charged FeOOH particles adsorb all ions that form anionic complexes such as $HPO4^{2-}$. In addition, the low charge density of the FeOOH surface enables the formation of covalent bonds with other slightly charged or neutral dissolved species such as $Ti(OH)_4{}^0$. In the second stage, both types of colloids eventually combine and precipitate forming typically hydrogenetic ferromanganese nodules with Mn+Fe contents around 50% unity (0% water and 0% pore space) (Figures 6b and 12b). After precipitation, Co and Ni are absorbed by Mn minerals, whereas Cu may be controlled by the different composition of the sediments. The fine diagenetic layers may be caused by the increased biological productivity of the surface ocean, which results in the reduction and dissolution of Mn oxides in sediment and release of associated elements (Figure 12d). These metals diffuse upwards and, on contact with oxygen-rich ocean water, are reoxidized, leading to the formation of diagenetic layers (high Mn/Fe ratio, Ni and Cu contents). Once oxic–suboxic front raised above the nodule, Mn, Ni, Co, and Cu were released into the pore water or seawater under suboxic conditions ($MnO_2$ in nodules was destroyed) and the remaining Fe oxyhydroxides reacted with products of the dissolution of siliceous ooze and clay minerals to form the Si-rich layer. (Figure 12e).

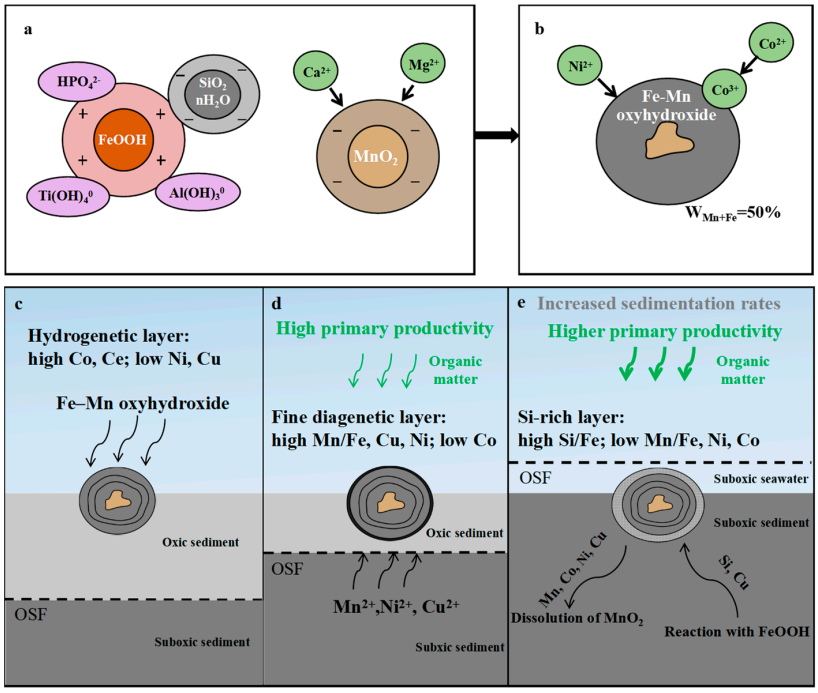



**Figure 12.** Model summarizing the main processes during the formation of the nodules in this study. (**a**,**b**): Two stages of the formation of hydrogenetic layers. (**c**–**e**): The schematic of formations of hydrogenetic, diagenetic, and Si-rich layers, with variations in chemistry. OSF = oxic–suboxic front. (**a**): OSF is deep, metals in pore water within suboxic sediments cannot diffuse to the bottom of the ferromanganese nodule to be adsorbed, which mainly experience oxic hydrogenetic processes; (**b**): OSF is near the bottom of the ferromanganese nodule and the metals of pore water within suboxic sediment can diffuse upward approaching the ferromanganese nodule; (**c**): OSF is above the ferromanganese nodule and dissolution of nodules occurs.

## 5. Conclusions

In this paper, we have recognized the diversity of hydrogenetic and diagenetic layers in the nodules from the Northwestern Pacific Ocean. Heterogeneous and complex textures characterize the internal growth structures of Fe–Mn nodules. Micrometer-scale measurements of metal abundances reveal complex element associations among the major elements, which are not resolvable via bulk analytical methods. The distributions of the major elements suggest that the growth of this hydrogenetic Fe–Mn nodule is likely controlled by the availability of Mn and Fe and the diversity of the environmental conditions such as changes of biological productivity of the surface ocean and sedimentation rates of surrounding sediment. In addition, we have shown that ultrafine-scale EMPA spot analysis in combination with other microscopic investigation techniques is a powerful way for high-resolution geochemical study on Fe–Mn nodules. The applications of EMPA and the associations between the elements could be useful for identifying environmental changes that occurred during the nodule growth.

**Supplementary Materials:** The following supporting information can be downloaded at: https://www.mdpi.com/article/10.3390/min13030415/s1, Figure S1: The cross sections of the nodules; Figure S2: Microscopic investigations and depth profiles of element contents of D07; Tables S1: Locations and depths of the samples; Tables S2–S4: Chemical compositions obtained by EMPA; Table S5: Trace element compositions obtained by ICP-MS.

**Author Contributions:** Conceptualization, C.L. and S.-J.K.; methodology, W.S.; software, C.L., Z.S. and X.Y.; formal analysis, C.L. and W.S.; investigation, C.L., W.H. and G.H.; resources, S.-J.K. and W.S.; data curation, W.S.; writing—original draft preparation, C.L.; writing—review and editing, S.-J.K. and W.S.; visualization, C.L.; supervision, W.S. and S.-J.K.; project administration, S.-J.K. and W.S. All authors have read and agreed to the published version of the manuscript.

**Funding:** This research was supported by grant 92058204 from National Natural Science Foundation of China (NSFC), grant DD20221720 and DD20190236 from China Geological Survey and grant KLSG2005 from Key laboratory of submarine geosciences, MNR.

**Data Availability Statement:** Data supporting the findings of this study will be made available from the corresponding author, upon reasonable request.

**Conflicts of Interest:** The authors declare no conflict of interest.

## References

1. Hein, J.R.; Koschinsky, A. Deep-Ocean Ferromanganese Crust and Nodules. In *Earth Systems and Environmental Sciences, Treatise on Geochemistry*, 2nd ed.; Holland, H., Turekian, K., Eds.; Elsevier: Amsterdam, The Netherlands, 2013; pp. 273–291.
2. Kuhn, T.; Wegorzewski, A.; Rühlemann, C.; Vink, A. Composition, Formation, and Occurrence of Polymetallic Nodules. In *Deep-Sea Mining: Resource Potential, Technical and Environmental Considerations*; Sharma, R., Ed.; Springer International Publishing: Berlin/Heidelberg, Germany, 2017; pp. 23–63.
3. Zhong, Y.; Chen, Z.; Hein, J.R.; González, F.J.; Jiang, Z.; Yang, X.; Zhang, J.; Wang, W.; Shi, X.; Liu, Z.; et al. Evolution of a deep-water ferromanganese nodule in the South China Sea in response to Pacific deep-water circulation and continental weathering during the Plio-Pleistocene. *Quat. Sci. Rev.* **2020**, *229*, 106106. [CrossRef]
4. Zhong, Y.; Liu, Q.; Chen, Z.; González, F.J.; Hein, J.R.; Zhang, J.; Zhong, L. Tectonic and paleoceanographic conditions during the formation of ferromanganese nodules from the northern South China Sea based on the high-resolution geochemistry, mineralogy and isotopes. *Mar. Geol.* **2019**, *410*, 146–163. [CrossRef]
5. Jiang, X.D.; Zhao, X.; Zhao, X.Y.; Chou, Y.M.; Roberts, A.P.; Hein, J.R.; Yu, J.M.; Sun, X.M.; Shi, X.F.; Cao, W.; et al. Abyssal manganese nodule recording of global cooling and Tibetan plateau pplift impacts on Asian aridification. *Geophys. Res. Lett.* **2022**, *49*, e2021GL096624. [CrossRef]
6. Koschinsky, A.; Halbach, P. Sequential leaching of marine ferromanganese precipitates: Genetic implications. *Geochim. Cosmochim. Acta* **1995**, *59*, 5113–5132. [CrossRef]
7. Koschinsky, A.; Hein, J.R. Uptake of elements from seawater by ferromanganese crusts: Solid-phase associations and seawater speciation. *Mar. Geol.* **2003**, *198*, 331–351. [CrossRef]
8. Glasby, G.P. Manganese: Predominant Role of Nodules and Crusts. In *Marine Geochemistry*; Schulz, H.D., Zabel, M., Eds.; Springer: Heidelberg, Germany, 2006; pp. 371–428.
9. Koschinsky, A.; Hein, J.R. Marine ferromanganese encrustations: Archives of changing oceans. *Elements* **2017**, *13*, 177–182. [CrossRef]

10. Wegorzewski, A.V.; Kuhn, T. The influence of suboxic diagenesis on the formation of manganese nodules in the Clarion Clipperton nodule belt of the Pacific Ocean. *Mar. Geol.* **2014**, *357*, 123–138. [CrossRef]
11. Blöthe, M.; Wegorzewski, A.V.; Müller, C.; Simon, F.; Kuhn, T.; Schippers, A. Manganese-cycling microbial communuties inside deep-sea manganese nodules. *Environ. Sci. Technol.* **2015**, *49*, 7692–7700. [CrossRef]
12. Halbach, P.; Friedrich, G.; von Stackelberg, U. *The Manganese Nodule Belt of the Pacific Ocean*; Enke: Stuttgart, Germany, 1988; pp. 61–69.
13. Wegorzewski, A.V.; Kuhn, T.; Dohrmann, R.; Wirth, R.; Grangeon, S. Mineralogical characterization of individual growth structures of Mn-Nodules with different Ni+Cu content from central Pacific Ocean. *Am. Mineral.* **2015**, *100*, 2497–2508. [CrossRef]
14. Su, R.; Sun, F.Y.; Li, X.H.; Chu, F.Y.; Sun, G.S.; Li, J.; Wang, H.; Li, Z.G.; Zhang, C.; Zhang, W.Y.; et al. Diverse early diagenetic processes of ferromanganese nodules from the eastern Pacific Ocean: Evidence from mineralogy and in-situ geochemistry. *Int. Geol. Rev.* **2022**, 1–17, *ahead of print*. [CrossRef]
15. Llovet, X.; Moy, A.; Pinard, P.T.; Fournelle, J.H. Electron probe microanalysis: A review of recent developments and applications in materials science and engineering. *Prog. Mater. Sci.* **2021**, *116*, 100673. [CrossRef]
16. Hein, J.R.; Spinardi, F.; Okamoto, N.; Mizell, K.; Thorburn, D.; Tawake, A. Critical metals in manganese nodules from the Cook Islands EEZ, abundances and distributions. *Ore Geol. Rev.* **2015**, *68*, 97–116. [CrossRef]
17. Guan, Y.; Sun, X.M.; Shi, G.Y.; Jiang, X.D.; Lu, H.F. Rare earth elements composition and constraint on the genesis of the polymetallic crusts and nodules in the South China Sea. *Acta Geol. Sin. Engl. Ed.* **2017**, *91*, 1751–1766. [CrossRef]
18. Knaack, D.; Sullivan, K.; Brown, D.; Langa, M.; Mathieu, J.; Bouchard, M.; Haring, M.; Petrus, J.; Stern, B.; Hein, J.; et al. Geochemical and mineralogical composition of ferromanganese precipitates from the southern Mariana arc: Evaluation, formation, and implications. *Chem. Geol.* **2021**, *568*, 120132. [CrossRef]
19. Ren, J.B.; Yao, H.Q.; Yang, Y.; Wang, L.X.; He, G.W.; Lai, P.X.; Zhou, J.; Deng, X.G.; Liu, S.J.; Deng, X.Z.; et al. Critical metal enrichment in atypical hydrogenetic ferromanganese nodules: A case study in the Central Basin Ridge of the West Philippine Basin. *Chem. Geol.* **2023**, *615*, 121224. [CrossRef]
20. Mclennan, S.M. Rare Earth Elements in Sedimentary Rocks: Influence of Provenance and Sedimentary Processes. In *Geochemistry and Mineralogy of Rare Earth Elements*; Lipin, B.R., McKay, G.A., Eds.; Mineral. Soc. Am.: Washington, MA, USA, 1989; Volume 21, pp. 169–200.
21. Chukhrov, F.V.; Gorshkov, A.I.; Beresovskaya, V.V.; Sivtsov, A.V. Contributions to the mineralogy of authigenic manganese phases from marine manganese deposits. *Miner. Depos.* **1979**, *14*, 249–261. [CrossRef]
22. Frondel, C.; Marvin, U.B.; Ito, J. New occurrences of todorokite. *Am. Mineral.* **1960**, *45*, 1167–1173.
23. Jones, L.H.P.; Milne, A.A. Birnessite, a new manganese oxide mineral from Aberdeenshire, Scotland. *Mineral. Mag.* **1956**, *31*, 283–288. [CrossRef]
24. Manheim, F.; Lane-Bostwick, C. Cobalt in ferromanganese crusts as a monitor of hydrothermal discharge on the Pacific sea floor. *Nature* **1988**, *335*, 59–62. [CrossRef]
25. Usui, A.; Nishi, K.; Sato, H.; Nakasato, Y.; Thornton, B.; Kashiwabara, T.; Tokumaru, A.; Sakaguchi, A.; Yamaoka, K.; Kato, S.; et al. Continuous growth of hydrogenetic ferromanganese crusts since 17 Myr ago on Takuyo-Daigo Seamount, NW Pacific, at water depths of 800–5500 m. *Ore Geol. Rev.* **2017**, *87*, 71–87. [CrossRef]
26. Ren, X.W.; Liu, J.H.; Shi, X.F.; Cui, Y.C.; Lin, X.H. Genesis and ore-forming stages of co-rich ferromanganese crusts from seamount m of magellan seamounts: Evidence from geochemistry and co chronology. *Mar. Geol. Quat. Geol.* **2011**, *31*, 65–74. [CrossRef]
27. Bonatti, E.; Kraemer, T.; Rydell, H. Classification and genesis of submarine iron-manganese deposits. In *Ferromanganese Deposits on the Ocean Floor*; Horn, D.R., Ed.; NSF: Washington, DC, USA, 1972; pp. 149–166.
28. Bau, M.; Schmidt, K.; Koschinsky, A.; Hein, J.; Kuhn, T.; Usui, A. Discriminating between different genetic types of marine ferro-manganese crusts and nodules based on rare earth elements and yttrium. *Chem. Geol.* **2014**, *381*, 1–9. [CrossRef]
29. Hein, J.R.; Koschinsky, A.; Kuhn, T. Deep-ocean polymetallic nodules as a resource for critical materials. *Nat. Rev. Earth Environ.* **2020**, *1*, 158–169. [CrossRef]
30. Halbach, P. Processes controlling the heavy metal distribution in pacific ferromanganese nodules and crusts. *Geol. Rundsch.* **1986**, *75*, 235–247. [CrossRef]
31. Dymond, J.; Lyle, M.; Finney, B.; Piper, D.Z.; Murphy, K.; Conard, R.; Pisias, N. Ferromanganese nodules from MANOP sites H, S, and R-control of mineralogical and chemical composition by multiple accretionary processes. *Geochim. Cosmochim. Acta* **1984**, *48*, 931–949. [CrossRef]
32. Halbach, P.; Giovanoli, R.; von Borstel, D. Geochemical processes controlling the relationship between Co, Mn, and Fe in early diagenetic deep-sea nodules. *Earth Planet. Sci. Lett.* **1982**, *60*, 226–236. [CrossRef]
33. Takahashi, Y.; Manceau, A.; Geoffroy, N.; Marcus, M.A.; Usui, A. Chemical and structural control of the partitioning of Co, Ce, and Pb in marine ferromanganese oxides. *Geochim. Cosmochim. Acta* **2007**, *71*, 984–1008. [CrossRef]
34. Wegorzewski, A.V.; Grangeon, S.W.; Samuel, M.; Heller, C.; Kuhn, T. Mineralogical transformations in polymetallic nodules and the change of Ni, Cu and Co crystal-chemistry upon burial in sediments. *Geochim. Cosmochim. Acta* **2020**, *282*, 19–37. [CrossRef]
35. Burns, V.M.; Burns, R.G. Authigenic todorokite and phillipsite inside deep sea manganese nodules. *Am. Mineral.* **1978**, *63*, 827–831.
36. Bodeï, S.; Manceau, A.; Geoffroy, N.; Baronnet, A.; Buatier, M. Formation of todorokite from vernadite in Ni-rich hemipelagic sediments. *Geochim. Cosmochim. Acta* **2007**, *71*, 5698–5716. [CrossRef]

37. Haeckel, M.; König, I.; Riech, V.; Weber, M.E.; Suess, E. Pore water profiles and numerical modelling of biogeochemical processes in Peru Basin deep-sea sediments. *Deep Sea Res. Part II* **2001**, *48*, 3713–3736. [CrossRef]
38. Heller, C.; Kuhn, T.; Versteegh, G.J.M.; Wegorzewski, A.V.; Kasten, S. The geochemical behavior of metals during early diagenetic alteration of buried manganese nodules. *Deep Sea Res. Part I Oceanogr. Res. Pap.* **2018**, *142*, 16–33. [CrossRef]
39. Ren, J.B.; He, G.W.; Deng, X.G.; Deng, X.Z.; Yang, Y.; Yao, H.Q.; Yang, S.X. Metallogenesis of Co-rich ferromanganese nodules in the northwestern Pacific: Selective enrichment of metallic elements from seawater. *Ore Geol. Rev.* **2022**, *143*, 104778. [CrossRef]
40. Kuhn, T.; Heller, C.; Kasten, S.; Koschinsky, A.; Versteegh, G.; Villinger, H. Niedrigthermale Fluidzirkulation an Seamounts und Störungszonen in 20 Mio. In Jahre alter ozeanischer Kruste: Ergebnisse der Expedition SO240-FLUM. Statusseminar "Meeresforschung mit FS SONNE". In Proceedings of the Tagungsband Zum Statusseminar 2017 Meeresforschung Mit FS Sonne, Oldenburg, Germany, 14–15 February 2017; pp. 30–34.
41. Müller, P.J.; Hartmann, M.; Suess, E. The chemical environment of pelagic sediments. In *The Manganese Nodule Belt of the Pacific Ocean Geological Environment, Nodule Formation, and Mining Aspects*; Halbach, P., Friedrich, G., von Stackelberg, U., Eds.; Ferdinand Enke Verlag: Stuttgart, Germany, 1988; pp. 70–90.
42. Stumm, W.; Morgan, J.J. *Aquatic Chemistry: An Introduction Emphasizing Chemical Equilibria in Natural Waters*, 3rd ed.; John Wiley & Sons Ltd.: New York, NY, USA, 1996; p. 1022.
43. Shen, X.; Wan, S.; France-Lanord, C.; Clift, P.; Tada, R.; Révillon, S.; Shi, X.; Zhao, D.; Liu, Y.; Yin, X.; et al. History of Asian eolian input to the Sea of Japan since 15 Ma: Links to Tibetan uplift or global cooling? *Earth Planet. Sci. Lett.* **2017**, *474*, 296–308. [CrossRef]
44. Rea, D.K.; Snoeckx, H.; Joseph, L.H. Late Cenozoic eolian deposition in the North Pacific: Asian drying, Tibetan uplift, and cooling of the northern hemisphere. *Paleoceanography* **1998**, *13*, 215–224. [CrossRef]
45. Guo, Z.; Ruddiman, W.; Hao, Q.; Wu, H.; Qiao, Y.; Zhu, R.; Peng, S.; Wei, J.J.; Yuan, B.; Liu, T.S. Onset of Asian desertification by 22 Myr ago inferred from Loess deposits in China. *Nature* **2002**, *416*, 159–163. [CrossRef]
46. Westerhold, T.; Marwan, N.; Drury, A.; Liebrand, D.; Agnini, C.; Anagnostou, E.; Barnet, J.; Bohaty, S.; De Vleeschouwer, D.; Florindo, F.; et al. An astronomically dated record of Earth's climate and its predictability over the last 66 million years. *Science* **2020**, *369*, 1383–1387. [CrossRef]
47. Atkins, A.L.; Shaw, S.; Peacock, C.L. Nucleation and growth of todorokite from birnessite: Implications for trace-metal cycling in marine sediments. *Geochim. Cosmochim. Acta* **2014**, *144*, 109–125. [CrossRef]


**Disclaimer/Publisher's Note:** The statements, opinions and data contained in all publications are solely those of the individual author(s) and contributor(s) and not of MDPI and/or the editor(s). MDPI and/or the editor(s) disclaim responsibility for any injury to people or property resulting from any ideas, methods, instructions or products referred to in the content.